



OPEN ACCESS

EDITED BY

Omid Haeri-Ardakani,
Department of Natural Resources
(Canada), Canada

REVIEWED BY

Yong Ma,
China University of Petroleum, China
Thomas Gentzis,
Core Laboratories, United States

*CORRESPONDENCE

Zecheng Wang,
wangzecheng@petrochina.com.cn

SPECIALTY SECTION

This article was submitted to
Sedimentology, Stratigraphy and
Diagenesis,
a section of the journal
Frontiers in Earth Science

RECEIVED 26 September 2022

ACCEPTED 02 November 2022

PUBLISHED 17 January 2023

CITATION

Li R, Xiong Z, Wang Z, Xie W, Li W and
Su N (2023), Lithofacies, mineralogy,
and pore characteristics of Permian
marine tuffaceous rocks in the
Sichuan Basin.
Front. Earth Sci. 10:1054276.
doi: 10.3389/feart.2022.1054276

COPYRIGHT

© 2023 Li, Xiong, Wang, Xie, Li and Su.
This is an open-access article
distributed under the terms of the
[Creative Commons Attribution License
\(CC BY\)](https://creativecommons.org/licenses/by/4.0/). The use, distribution or
reproduction in other forums is
permitted, provided the original
author(s) and the copyright owner(s) are
credited and that the original
publication in this journal is cited, in
accordance with accepted academic
practice. No use, distribution or
reproduction is permitted which does
not comply with these terms.

Lithofacies, mineralogy, and pore characteristics of Permian marine tuffaceous rocks in the Sichuan Basin

Rong Li^{1,2}, Zhifu Xiong³, Zecheng Wang^{1,2*}, Wuren Xie^{1,2},
Wenzheng Li⁴ and Nan Su^{1,2}

¹Research Institute of Petroleum Exploration & Development, PetroChina, Beijing, China, ²CNPC Key Laboratory of Natural Gas Accumulation and Development, Langfang, China, ³Sinopec Exploration Company, Chengdu, China, ⁴Hangzhou Research Institute of Geology, Hangzhou, China

Alongside volcanic eruptions in the middle and late Permian, the sedimentary environment and process changed, and the lithofacies and mineralogical characteristics varied conspicuously from the marine sediments in this period. Marine tuffaceous rocks beared strong witness to the marine and volcanic actions in this time. With experimental studies relying on field outcrop, thin section, scanning electron microscope, X-ray diffraction (XRD), mercury injection capillary pressure (MICP) and CT scan, the researchers analyzed the lithology, mineralogy, and pore characteristics of marine tuffaceous rocks. Among the Permian marine tuffaceous sections of the Sichuan Basin, three types of lithofacies were identified, namely tuff, sedimentary tuff, and tuffaceous mudstone. The mineral composition of the tuffaceous section includes quartz, feldspar, carbonate minerals, pyrite, clay, etc. The quartz content varies from 4.0% to 27.3%, with an average value of 13.0%; the feldspar content varies from 0 to 21.2%, with an average value of 9.8%; the carbonate mineral content varies from 8.52% to 53.45%, with an average value of 27.6%; the clay mineral content varies from 0 to 75.3%, with an average value of 44.8%; and the pyrite content varies from 0 to 13.4%, with an average value of 5.8%. The porosity of tuffaceous rocks varies from 2.2% to 8.1%, mostly concentrated in the range from 3% to 7% with an average level of 5.24%. There are mainly shrinkage pores, dissolution pores, intercrystalline pores, and organic pores. In terms of scale, the pores can be classified as micron-scale and nano-scale pores, and in terms of size, they are mainly micropores and mesopores, accounting for up to 92.12%. The pores are concentrated in the tuffaceous section and well interconnected, forming a complex organic-inorganic pore-fracture network system and bedding fractures with even better connectivity. The pores of the tuffaceous section are greatly influenced by lithofacies and mineral composition. The porosities of tuffaceous mudstone, sedimentary tuff and tuff rank downward, with average porosities of 6.5%, 5.09%, and 3.86% respectively. The felsic content is inversely correlated with porosity; the clay content and TOC content are positively correlated with porosity; the pyrite content is also inversely correlated with porosity. The marine tuffaceous section is similar to shale to a certain extent as it has relatively dense lithology, its pores are mainly of micron-scale

and nano-scale and mainly include micropores and mesopores. It boasts the hydrocarbon-generating capacity and reservoir performance, serving as both a source rock and a reservoir. As a novel reservoir, the tuffaceous section can form a tight reservoir both generating and depositing gas and featuring source-reservoir paragenesis, lithological reservoir-controlling, and large-area stratified distribution, manifesting a promising future for exploration.

KEYWORDS

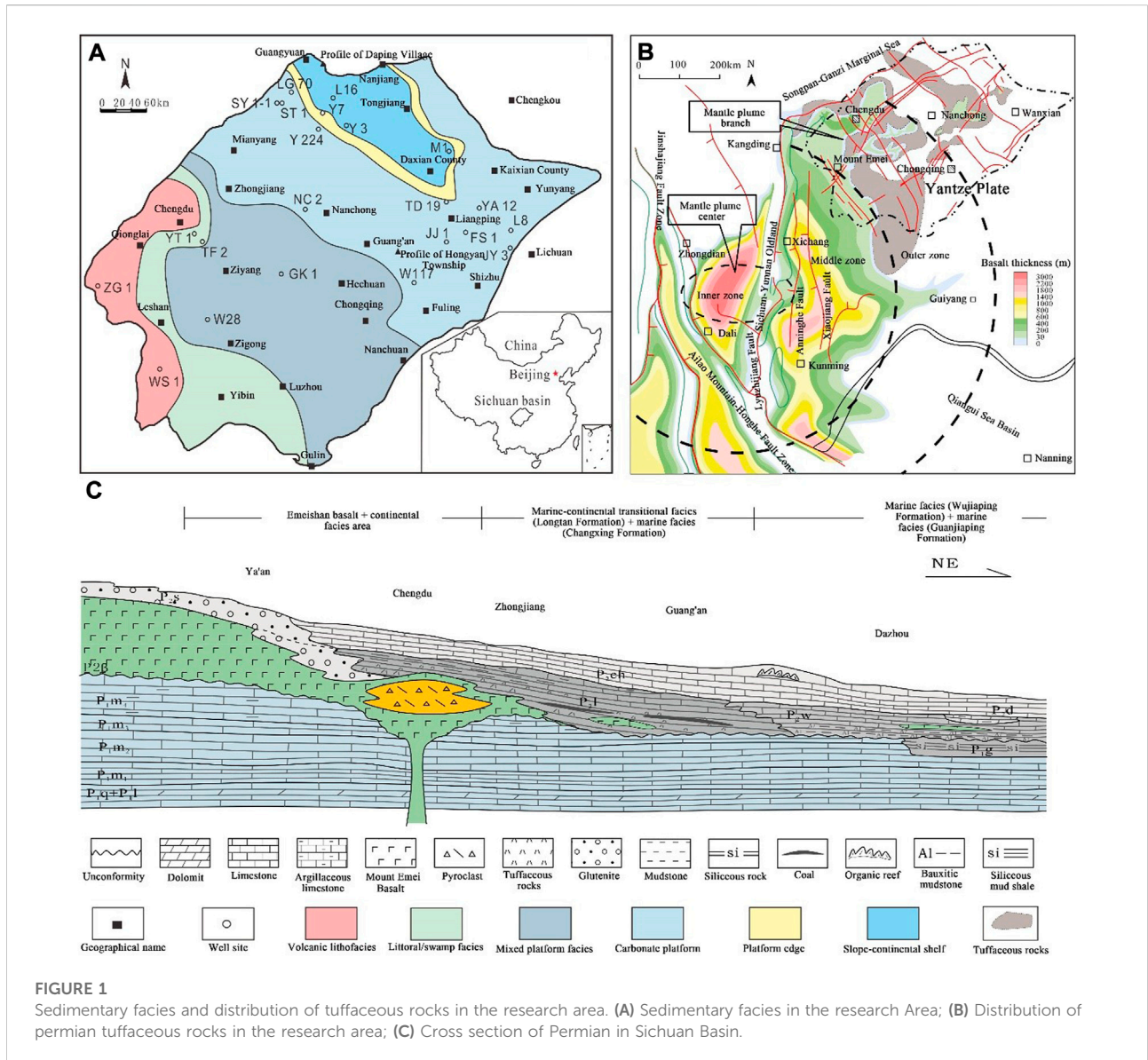
tuff, sedimentary tuff, tuffaceous mudstone, lithology, mineralogy, pore characteristics

1 Introduction

In recent years, pyroclastic rock reservoirs have been discovered successively in some sedimentary basins in Japan, Cuba, The United States, New Zealand and Turkey, as well as in the Ordos Basin, the Junggar Basin, the Jiuquan Basin, the Bohai Bay Basin, the Erlian Basin, and the Songliao Basin in China, drawing much attention to the exploration of pyroclastic rock oil and gas (Vernik, 1990; Cao et al., 1999; Levin, 1995; Schutter, 2003; Gecer, 2006; Ma et al., 2019a; Zhang et al., 2019). The formation testing of the pyroclastic rock reservoir in Member II of the Middle Permian Tiaohu Formation, the Malang Depression and the Santanghu Basin carried out successfully in 2013 confirmed the importance of a new type of reservoir - tight tuff reservoir and opened up a new field of oil and gas exploration in China.

During the mid-late Permian of the late Paleozoic, the marine sedimentary environment and sedimentary process changed. A volcanic eruption occurred in southwest China, forming the Emeishan Large Igneous Province (ELIP) recognized by the international academic circles (Huang and Opdyke, 1998; Zhou et al., 2001; Ali et al., 2002; Zhang, 2006; Zhong et al., 2007; Peate and Bryan, 2008; Hong et al., 2009; Wignall et al., 2009; Shellnutt et al., 2012; Zhu and Zhang, 2013; Tian et al., 2017). It is composed of massive basalt with overflow facies, pyroclastic lava with extrusive facies, and tuffaceous rocks with volcanic sedimentary facies (Ma et al., 2019a; Wen et al., 2019; Liu et al., 2020). At the end of the 20th century, vertical Well ZG1 drilling 301.5 m basalt in Permian System revealed in the logging a 14.6 m fractured reservoir (naturally fractured reservoir) with a daily gas production of 256,100 m³ according to the test. Recently, vertical Well YT1 at Longquanshan tectonic belt in the west of the Sichuan Basin drills into a pored reservoir of pyroclastic lava in the Permian volcanic section, which reveals a rich gas deposit promising a daily production of 225,000 m³ industrial gas run, while vertical Well Y7 located in the north of Sichuan Province encounters a tight lay at the tuffaceous section in the Permian volcanic section, promising a daily production of 1.05 million m³ industrial gas run (Industrial gas flow standards refer to the new Petroleum and Natural Gas Reserves Specification after 1990) (Hu, 2019; Wen et al., 2019; Tian et al., 2021). These results indicate the great potential in the exploration of Permian pyroclastic rocks in the Sichuan Basin.

According to the Permian drilling results in the Sichuan Basin, a compact layer of tuffaceous section is developed in the Permian system of Well Y7 and shows good reservoir quality, varying greatly from the fractured reservoir of basalt and pored reservoir of pyroclastic lava found earlier (Hu, 2019; Wen et al., 2019). Previous researchers believed that basalt and pyroclastic lava in the basin contain rich deposits but paid less attention to marine tuffaceous sections. Pyroclastic rocks, especially those underwent strong diagenetic transformation, are difficult to identify protolith type, and this is why Permian pyroclastic rocks in drilling in the Sichuan basin were rarely reported in the past. In addition, previous studies on pyroclastic have mainly focused on lacustrine deposits, and research examples on identification and characterization of marine tuff and sedimentary tuff, especially on the scale of drilling cuttings and cores, are rare. The understanding of the overall situation and the characteristics such as the lithology, mineralogy, and pore characteristics of marine tuffaceous rocks are inadequate, which hinders the exploration and development of the Permian marine tuff reservoirs in the Sichuan Basin (Ma et al., 2019b; Wen et al., 2019; Liu et al., 2020; Tian et al., 2021). Previous studies on lithofacies focus on the sedimentary structure, biological characteristics, and organic matter and mineral composition of rocks. Among them, mineralogical analysis features prominently in identifying the sedimentary and reworking process of rocks in the later period (Altaner and Ylagan, 1997; Freundt, 1999; Chen et al., 2016; Hickey and Henk, 2007; Zhang et al., 2008; Christidis and Huff, 2009; Syed and Padmanabhan, 2022). Tuffaceous rock, a transition rock between volcanic rock and sedimentary rock, differs from the latter in terms of its lithological characteristics and mineral composition. It is greatly affected by volcanic alteration and later sedimentary-reworking processes (Streck et al., 1995; Colin and Wes, 2003; Inoue et al., 2004; Ddani et al., 2005; García-Romero et al., 2005; Wang et al., 2005; Bertog et al., 2007; Liu et al., 2007; Carey, et al., 2008; Cheng et al., 2010; Yanik et al., 2010; Wang et al., 2020; Xiang et al., 2021; Fan et al., 2022; Li et al., 2022). To identify the basic characteristics of the tuffaceous section, the author studied the Upper Permian marine tuffaceous rocks in the Sichuan Basin by thin-section identification, scanning electron microscopy and energy dispersive spectroscopy (SEM-EDS), X-ray diffraction analysis (XRD), mercury injection capillary



pressure (MICP), CT scan and other means. In the study of the lithic fragments and cores, the author observed the macro-sedimentary structure and microscopic characteristics and analyzed its lithofacies characteristics considering the mineral composition and content. The pore characteristics of this compact layer under lithofacies control were investigated in a bid to provide a reference for future exploration of this new type of Permian marine tuffaceous rocks.

The intercalated tuffaceous in the adjacent Shangsi area, Guanyuan, in the late Permian strata, have been proved to be related to the ELIP (Huang et al., 2018). Therefore, tuffaceous deposits in the study area also can constraint the time and influence range of magmatic activities of ELIP. It will have a profound impact on the study of Permian global climate change and the mass extinction event.

2 Regional geological background

In the middle and late Permian, the Sichuan Basin experienced the Dongwu Movement and the Emei Taphrogeny. Under the influence of such movements, the stratigraphic differentiation in this period was conspicuous, seeing the basalt formation of Mount Emei in southwest Sichuan; Longtan Formation, a coal-bearing stratum of transitional facies, in middle-southern Sichuan; and Wujiaping Formation, a stratum of carbonate rocks coupled with shale of abysmal facies, in eastern and northern Sichuan, in unconformable contact with the underlying Maokou Formation. This period witnessed a variable overall sedimentary environment and complicated lithology. The plane has the volcanic facies, littoral/swamp facies, mixed

platform facies, carbonate platform facies, and slope facies (Figure 1A) developed from west to east (Tian et al., 2010; He et al., 2015; Tian, 2018).

Volcanic lithofacies distributed in large areas within the Sichuan Basin falls into three types: overflow facies, extrusive facies, and volcanic sedimentary facies. Overflow facies refers to lava basalt during volcanic activity, which exists as rock flow and rock quilt in large areas and is mainly distributed in the Ya'an-Leshan-Pingshan region in southwest Sichuan. It is formed by magma overflowing into the basin from the main basalt zone of Mount Emei with its thickness thinning from southwest to northeast, where the basalt thickness gradually decreases from approximately 600 m to zero within 100 km. The extrusive facies, mainly composed of pyroclastic lava (breccia lava, tuffaceous breccia lava, and lava containing tuffaceous breccia), features low viscosity and good fluidity and is mainly distributed in the Chengdu-Jianyang region, with a thickness of 200–350 m, thinning to below 50 m towards the edge. Volcanic sedimentary facies is a facies belt that transits from volcanic facies to sedimentary facies, and also a marine tuffaceous section, formed by re-sedimentation of volcanic debris after being moved by ocean currents. Its rocks are thin, normally with sedimentary bedding and structure. It is widely distributed in the Sichuan Basin (Figures 1B,C) (Xia et al., 2020; Zeng et al., 2020; Peng et al., 2022).

3 Materials and methods

We collected data from the Hongyan Township profile, the Daping Village profile (Shuanghui Town, Wangcang County), and Well Y7, with an average sampling interval of less than 1 m. It contains 87 data, including 27 from the Hongyan Township profile, 49 from Well Y7, and 11 from the Daping Village profile, mainly used for TOC and mineral composition analysis.

The analysis of thin sections and SEM was carried out in the Key Laboratory of Petroleum Geochemistry of China National Petroleum Corporation (CNPC) by Nikon Eclipse LV100POL polarizing microscope and FEIQUANTAN 250 FEG scanning electron microscope. XRD analysis was carried out in the State Key Lab of Oil & Gas Reservoir Geology and Exploitation, Chengdu University of Technology by using a Bruker D8 Advance diffractometer with Cu K α radiations, LynxEye XE detector and Ni filter, under 40 kV voltage and 40 mA intensity. Bulk mineralogy was studied using randomly orientated powders of the bulk samples and quantitative estimation of the bulk mineralogy used the method of Chung (1974). Clay minerals were studied on oriented mounts of non-calcareous clay-sized particles. Deflocculation was accomplished by successive washing with distilled water after decarbonation with 0.2 N HCl, and then particles finer than 2 μ m were concentrated by centrifugation (Deconinck et al., 2014). Three XRD runs were performed, respectively after air-drying (AD), ethylene-glycol solvation (EG), and heating at 490°C during 2 h.

Identification of clay minerals was made according to a comprehensive comparison of the three XRD diffractograms. The relative contents of each clay mineral species were estimated mainly according to the position and the area of (001) series of basal reflections (Moore and Reynolds, 1998).

4 Test results

4.1 Observation of core samples

In the observation of the Hongyan Township profile in east Sichuan, it is found that the top weathering crust of Maokou Formation that contacts Longtan Formation shows obvious darkened edges of burning, and the overlying Longtan Formation sees conspicuous elliptical and round breccia with a particle size from 25 mm to 1 cm, thinning from bottom up. Breccia is composed of limestone breccia, tuff breccia, and aphanitic siliceous breccia, dominated by siliceous breccia, with tuff developed between breccia (Figures 2A,B). On this sedimentary volcanic breccia develops a set of brown, thin sedimentary tuff intercalated with extremely thin tuffaceous mudstone, with interbedding and good stratification. Above the interbedding section of sedimentary tuff and tuffaceous mudstone lies a set of thick brownish-gray tuffaceous mudstone, with a developed horizontally-laminated bed, in stable distribution, and with good stratification. Holistically, the particle size of sediments decreases from the bottom up, stratification improves, with dragonfly fossils and bioclasts occasionally spotted (Figure 2).

Under the microscope, most rocks in the tuffaceous section are pyroclastic, argillaceous, and carbonate minerals in uneven distribution. Pyroclast mainly includes vitric fragments, quartz, feldspar crystal fragments, and lithic fragments. Most feldspar is argillized. Most crystal fragments and lithic fragments are devitrified into clay, and some are replaced by crystal powder dolomite. Carbonate minerals contain a small amount of dolomite and calcite, usually less than 6%, which cement pyroclastic grains. The euhedral crystal of dolomite is rarely spotted. The pyroclast particle size varies greatly, mostly concentrated in the range from 0.1 mm to 0.5 mm. The lithic fragments, with a particle size of generally over 0.050 mm and up to 0.500 mm at most, are mainly in round shape and partly in irregular shape and composed of rhyolite, tuff lithic fragments and hyaloclastite. The crystal fragments are dominated by quartz crystal fragments, with a small quantity of feldspar and mica crystal fragments. They are often in angular and fragmented shapes, with a particle size from 0.100 to 0.050 mm. The vitric fragments, with a particle size from 0.100 to 0.050 mm, are rarely in rigid fractures in the shape of chicken bone and crescent, but plastic shapes such as extruded or elongated deformation are common (Figure 3).

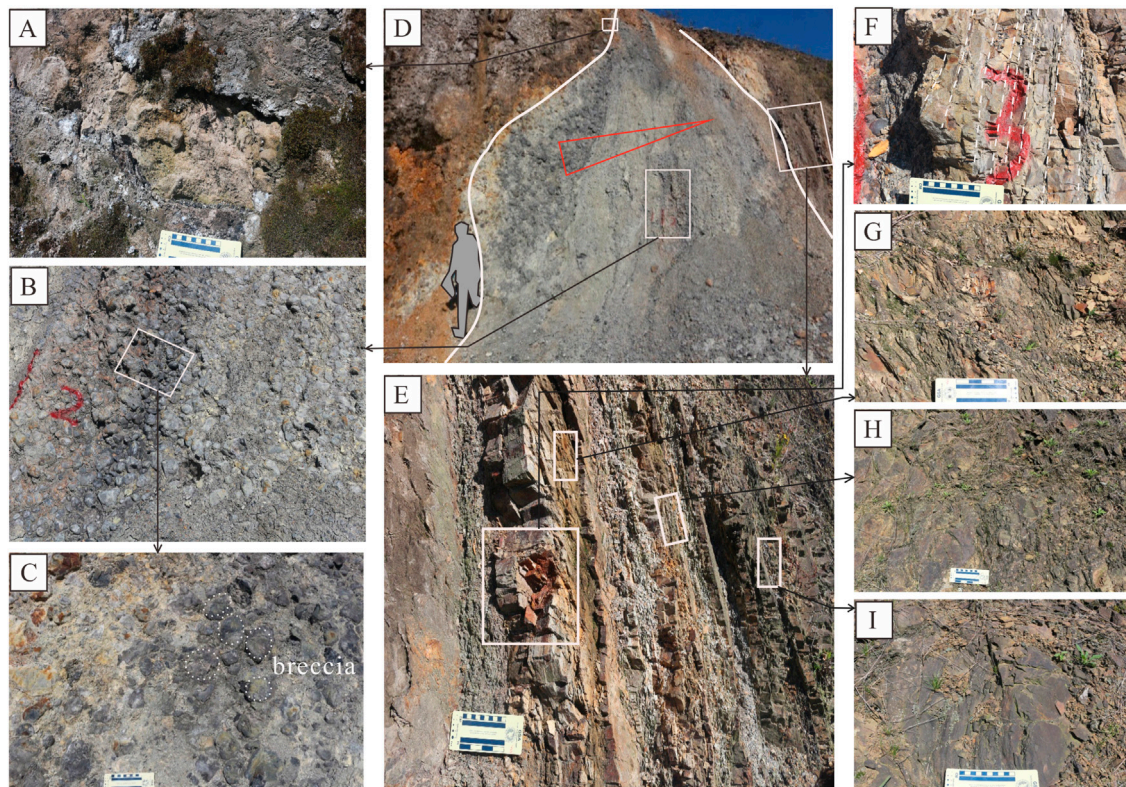


FIGURE 2

Typical lithological characteristics of longtan formation. (A): weathering crust on top of Maokou Formation, with darkened edges of baking; (B): brown sedimentary volcanic breccia intercalated with tuff for Longtan Formation, seeing elliptic or round breccia; (C): partial zoom-in of picture B, showing most siliceous breccia, with tuff between breccia; (D): full view of the Hongyan Township profile, showing the top of Maokou Formation and the bottom of Longtan Formation, with breccia of Longtan Formation decreasing from the bottom up (in the red triangle); (E): interbedding of brown sedimentary tuff and tuffaceous mudstone for Longtan Formation, with good stratification; (F): partial zoom-in of Picture E, showing thin, brown sedimentary tuff, with good stratification; (G): partial zoom-in of Picture E, showing very thin, brown tuffaceous mudstone, with good stratification; (H): partial zoom-in of Picture E, showing thin, brown sedimentary tuff; (I): partial zoom-in of Picture E, showing the top brown tuffaceous mudstone, with good stratification.

During core observation in the field, it is found that the tuffaceous section is often dense, where visible dissolution holes are not developed, and a few bedded cracks are spotted. The researchers observed by thin sections and scanning electron microscope that the tuffaceous section has abundant pore types, including shrinkage pores between mica and clay sections (Figure 4A), shrinkage pores in clay minerals (Figure 4B), irregular dissolution pores or circular mold pores formed in the dissolution of carbonate minerals or pyroclast (Figure 4C), intercrystalline pores between minerals (Figure 4D), micropores in organic matters (Figure 4E), and microcracks (Figure 4F). Among them, the shrinkage pores are mainly flat and elongated, generally with a width of tens to hundreds of nanometers; dissolution pores and mold pores are often filled with clay, and microcracks along the bedding are relatively developed and are often in an orientation direction consistent with that of the clay mineral aggregates.

4.2 Quantitative analysis of minerals

The whole-rock XRD results of the 87 samples show that minerals in the tuffaceous section mainly consist of clay, quartz, plagioclase, potash feldspar, calcite, dolomite, ankerite, and pyrite (Figure 5). Among them, quartz minerals content values vary from 4.0% to 27.3%, averaging 13.0%, with their content subject to regular change (increasing from the bottom up) in the typical well profile (Figure 5); clay minerals, mainly illite/smectite formation and illite, vary from 0% to 75.3%, averaging 44.8%, without samples containing zero clay minerals, seeing a content decreasing from the bottom up, contrary to quartz; feldspar minerals include potash feldspar and plagioclase, varying from 0 to 21.2%, averaging 9.8%, of which the plagioclase content is stable, while potash feldspar is not more than 1%; carbonate minerals mainly comprise calcite and dolomite, partially seen a high content of ankerite, ranging from 8.52% to 53.45%, with an

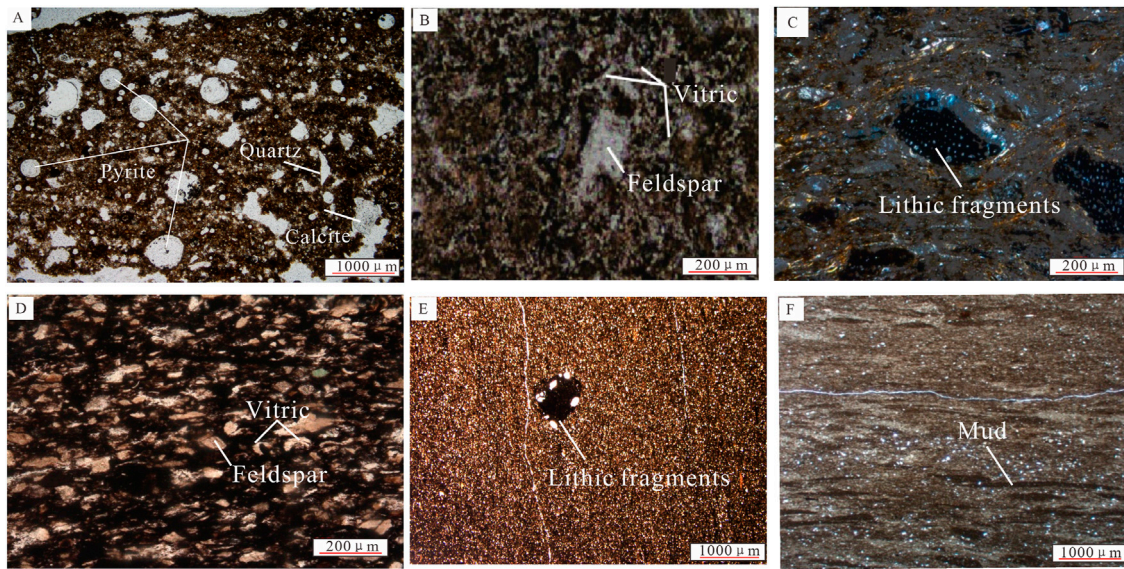


FIGURE 3

Thin section characteristics for typical lithology of longtan formation/wujiaping formation. (A): Well FS1, Wu No. 2 section, 4,832 m, tuff in lithic fragments, with quartz crystal fragments and pyrite, volcanic ash cementation; (B): Well Y7, Wu No. 2 section, 6,915 m, tuff in crystal fragments, with feldspar crystal fragments, vitric fragment de-vitrification, volcanic ash cementation; (C): Well TF2, Longtan Formation, 5,158.16 m, sedimentary tuff, with large lithic fragment and in an obvious tuffaceous structure; (D): Well NC2, Longtan Formation, 5,869 m, sedimentary tuff, with feldspar crystal fragments and vitric fragments; (E): Well ST1, Wu No.2 section, 6,725 m, tuffaceous mudstone, with large lithic fragments; (F): bottom of Longtan Formation for Huaying Mountain profile, tuffaceous mudstone, in stripes.

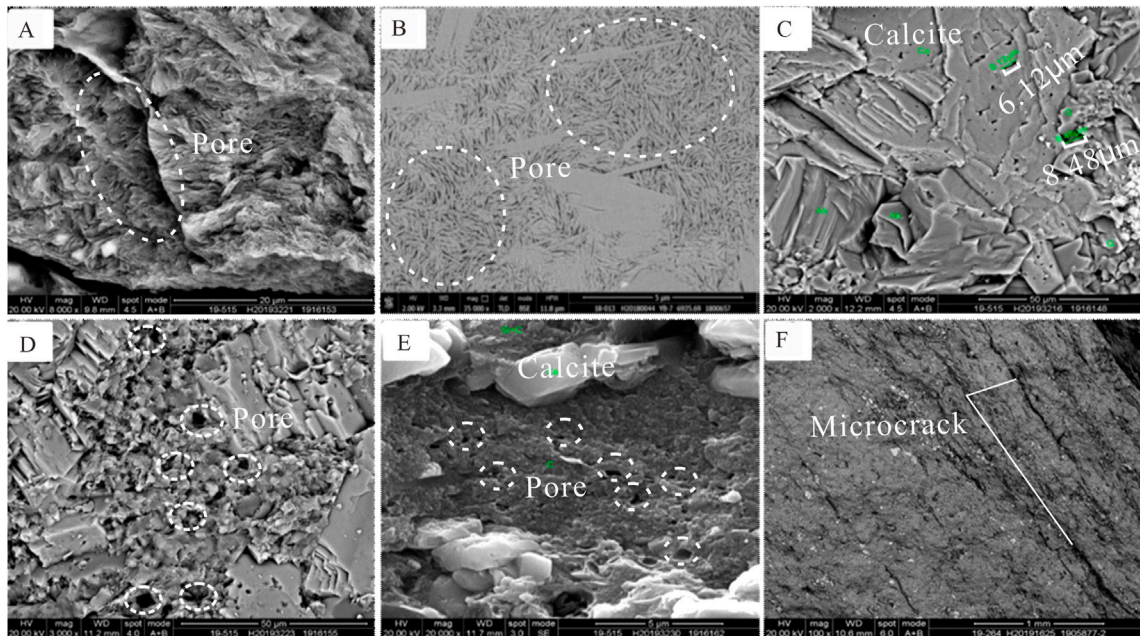


FIGURE 4

Typical reservoir space of tuffaceous section. (A) tuff, shrinkage pores developed between mica and clay sheets, 6,811.9 m, Well SY1-1; (B) Tuffaceous mudstone, shrinkage pores of clay mineral, 6,935.69 m, Well Y7; (C) sedimentary tuff, with enlarged calcite dissolved pores (below 6 microns), quartz and albite cemented in intercrystalline pores, 4,945.65 m, Well M1; (D) sedimentary tuff, intercrystalline pores developed for siderite, 6,867.21 m, Well SY1-1; (E) sedimentary tuff, organic pores developed, 6,867.21 m, Well SY1-1; (F) Tuffaceous mudstone, crack developed, 6,936.07 m, Well Y7.

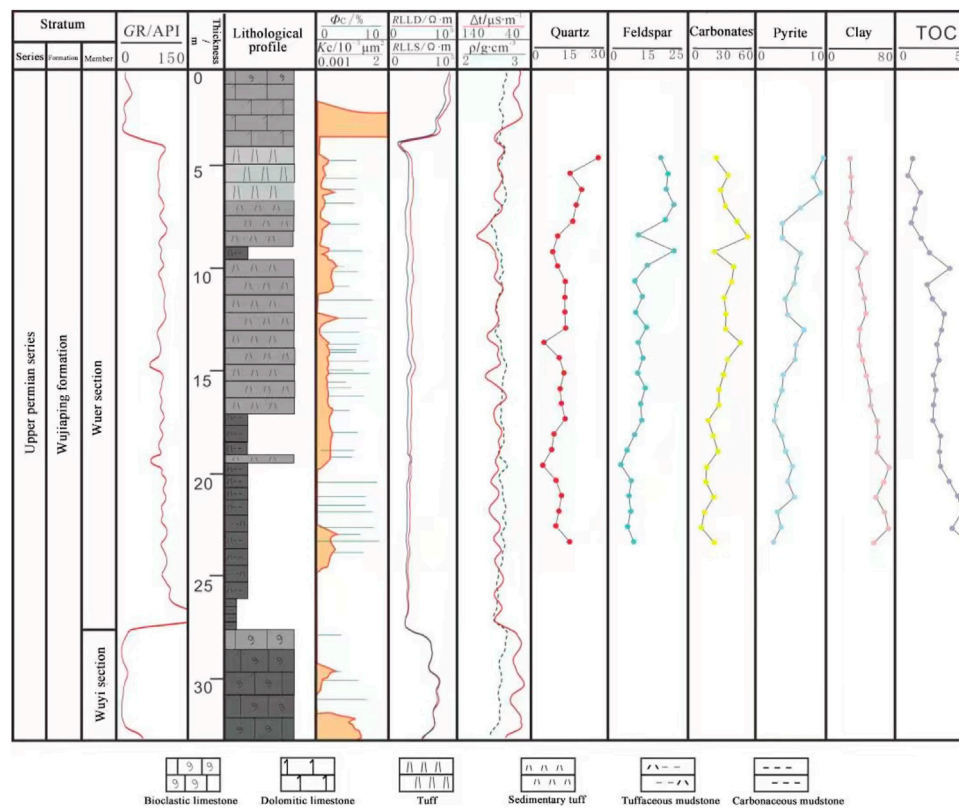


FIGURE 5
Main mineral composition of tuffaceous section of Y7 wells.

average of 27.6% and their content gradually drops from the bottom up on the profile. Pyrite can be detected in almost all drilled samples, with its content ranging from 0 to 13.4%, with an average of 5.8%.

According to the XRD data of clay, clay minerals, mainly composed of illite/smectite formation and illite, contain a small amount of chlorite. The illite/smectite formation has a high content, which ranges from 37% to 99% (Figure 6).

4.3 TOC

According to 87 organic carbon test data from the Hongyan Township profile, Daping Village profile, and Well Y7, the tuffaceous section contains organic carbon varying from 0.30% to 4.66%, averaging 2.48%, and most samples have a TOC ranging from 1% to 4% (Figure 5). The average TOC values for the Hongyan Township profile, Daping Village profile, and Well Y7 are 2.36%, 2.51%, and 2.52% respectively. According to the typical well Y7 in Figure 5, the low TOC value appears at the top of the tuffaceous rock section and the high TOC value appears at

the bottom of the tuffaceous rock, showing increasing trends from the top toward the bottom.

5 Discussion

5.1 Lithology

Pyroclastic rock with volcanic sedimentary facies developed in the research area belongs to the tuffaceous section, a transitional type transforming from normal pyroclastic rock into sedimentary rock. Referring to the classification and naming principles of volcanoclastic rocks (Schmid, 1981), and combining the classification standards of predecessors in the study area (Zhao, 2019; Li et al., 2020), through electrical characteristics, thin section and scanning electron microscope observation, combined with the whole rock X-ray diffraction characteristics, the tuffaceous rock sections in the study area can be divided into three categories: tuff, sedimentary tuff and tuffaceous mudstone (Table 1). In this area, normal pyroclastic rock is dominated by tuff, sedimentary pyroclastic rock by sedimentary tuff, and pyroclastic sedimentary rock by tuffaceous mudstone. The last two types of

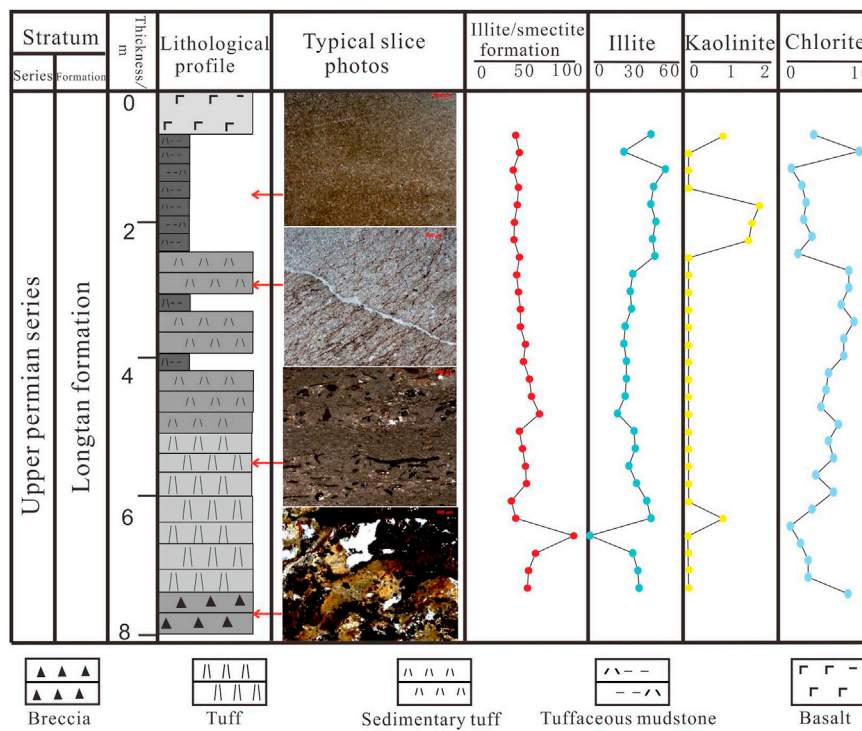


FIGURE 6 XRD Data of Clay for Tuffaceous Section of Hongyan Township profile.

TABLE 1 Classification of permian tuffaceous section in the sichuan basin.

Type	Rock	Composition	Sedimentary structure
Normal pyroclastic rock	Tuff	90%> pyroclastic material> 75%, particle size 0.05 0.5 mm	Inconspicuous stratified structure
Sedimentary pyroclastic rock	Sedimentary tuff	75%> pyroclastic materials >50%, terrigenous clast <50%	Conspicuous stratified structure
Pyroclastic sedimentary rock	Tuffaceous mudstone	Clay minerals >50%, pyroclast >10%	Conspicuous stratified structure

rocks see a conspicuous stratified structure. A small number of bioclasts, including spicule and foraminifer, can be seen locally, and silicification were spotted inside some of the bioclasts. The whole tuffaceous section, characterized by high gamma, long interval transit time, and low resistance, differs largely from other rocks. Tuffaceous rock has a natural gamma value between 65 and 145 API, compensation neutron value between 20 and 40 P•U, and interval transit time between 62 and 102 μs/ft; limestone has a natural gamma value between 14 and 55 API, compensation neutron value between 0 and 2 P•U, and interval transit time between 44 and 61 μs/ft; argillaceous limestone has a natural gamma value between 35 and 280 API, compensation neutron value between 2 and 10 P•U, and interval transit time between 50 and 76 μs/ft.

5.1.1 Tuff

Tuff is mainly gray, with more than 75% pyroclast, fine-medium grained texture of a particle size between 0.05 and 0.5 mm, and natural gamma-ray (GR) value between 65 and 110 API units, averaging 85 API units. Based on the results of thin section analysis over a colossal quantity of cores, we found out that tuff contains 75%–90% (or higher) of volcanic lithoclast, quartz, and feldspar. The lithic fragments see irregular edges and complicated shapes (in angular, sickle, bow, and crescent), disorderly placed, with loose appearance, coarse, porous, and most blocky. Whole-rock XRD shows that the felsic content of tuff varies from 18.7 to 43.76%, with an average value of 33.4%; the clay content is between 18.51 and 24.42%, with an average value of 23.11%.

TABLE 2 Characteristics of pore and fissure in SEM.

Sample number	Type and areal porosity (%) of pore and fissure				Image-based porosity (%)	Micropore (%)	Nanopore (%)	Fissure rate (%)	Fracture width (μm)
	Shrinkage pore	Solution pore	Intercrystalline pore	Organic pores					
SEM 1	7				7		100		
SEM 2	8				8	70	30		
SEM 3		1	2		3	65	35		
SEM 4		0.2	10		10.2	80	20		
SEM 5		0.2	2.5	2	4.7	10	90		
SEM 6			2		2	50	50	2	10
SEM 7		1.5	4		5.5	50	50	5	50
SEM 8				3	3	20	80		
SEM 9	10				10		100		
SEM 10	6		4		10	60	40		

5.1.2 Sedimentary tuff

Sedimentary tuff is mainly dark gray, with 50%–75% pyroclast, fine-grained texture of a particle size smaller than 0.1 mm, and natural gamma-ray (GR) value between 69 and 120 API units, averaging 93 API units. Based on the results of thin section analysis over a colossal quantity of cores, we found out that sedimentary tuff contains 50%–60% of volcanic lithoclast, quartz, feldspar, and 30%–40% of clay. Most clay minerals are altered from pyroclast. Sedimentary tuff shows a conspicuous stratified structure. Whole-rock XRD shows that the felsic content of the sedimentary tuff varies from 12.72 to 29.25%, with an average value of 21.89%; the clay content is between 24.42 and 49.44%, with an average value of 42.84%.

5.1.3 Tuffaceous mudstone

Tuffaceous mudstone, mostly grayish-black, is composed of pyroclast and sedimentary clast. Pyroclast has a low fraction, less than 50%, and has an appearance that looks more angular than sedimentary clast, thus uneasy for sorting and rounding. Its natural gamma-ray (GR) value ranges between 92 and 145 API units, averaging 109 API units. Based on the results of thin section analysis over a colossal quantity of cores, we found out that tuffaceous mudstone contains more clay (over 50%) and less volcanic lithoclast, quartz, and feldspar (below 50%). Whole-rock XRD shows that the felsic content of the tuffaceous mudstone varies from 6.29 to 30.5%, with an average value of 16.08%; the clay content is between 50.76 and 75.29%, with an average value of 64.06%.

The analysis of profile and coring data indicates that sedimentary tuff and tuffaceous mudstone often occur in a horizontally-laminated bed with alternate light and dark colors, whose thickness varies largely, where the thinnest layer

can be calculated in mm, while thick layers can reach 10 cm. The core can see pyrite enrichment in part, mostly blocky and partially in laminated distribution. Pyrite has different sizes, between 1 mm and 5 cm, unevenly distributed.

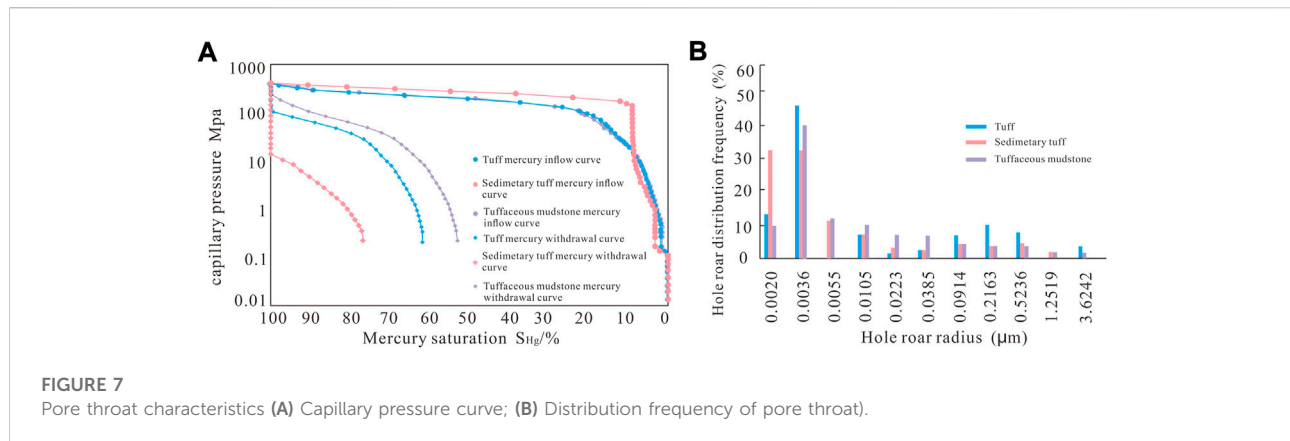
5.2 Pore characteristics

The pore characteristics of tuffaceous rocks are analyzed and clarified from the aspects of pore type, pore size distribution, and connectivity.

5.2.1 Pore types

The identification results of pores and seams in SEM show that (Table 2), the image-based porosity is between 1.5% and 10.2%, calculated by Avizo software, and the pores have certain connectivity. The main pore is shrinkage pore in tuffaceous rock section, and the maximum porosity is 10%; The next is intergranular pore, and the local layer can reach 10.0%. The porosity of organic matter is between 2% and 3%, while the porosity of dolomite dissolved pores is generally between 0.2% and 1.5%. The surface crack rate of the crack is between 2.0% and 5.0%, and between 10 and 50 μm wide crack can be seen in the scanning electron microscope.

Shrinkage pore: Shrinkage pores in the tuffaceous section have two genetic types. In the first case, pyroclast evolves toward stable minerals, such as quartz and feldspar, during the devitrification process, leading to volume shrinkage and forming shrinkage pores. Second, pyroclast turns into clay minerals during the metasomatic alteration process, while clay minerals have a shrunk diagenetic volume to form shrinkage pores. Whereas widely distributed in tuff, sedimentary tuff, and tuffaceous mudstone, shrinkage pores are most common in



tuffaceous mudstone. They are mainly flat and elongated, generally with a width of tens to hundreds of nanometers; Dissolution pore mainly includes intergranular and intragranular dissolution pores. During the metasomatic alteration of pyroclast, unstable minerals in feldspar and carbonate, prone to corrosion, form dissolution pores within feldspar and carbonate minerals. Dissolution pores are mostly irregular and widely distributed, with the pore sizes varying from 0.001 mm to 0.5 mm, and some pores are impregnated by organic matters later.

Intercrystalline pore: During de-vitrification, quartz and feldspar are generated, and mineral crystals are re-arranged to form intercrystalline pores, which may also occur during the formation of secondary minerals and carbonates in the metasomatic alteration process. Intercrystalline pores are often in triangular and irregular shapes between crystalline particles.

Organic pores: During metasomatic alteration and de-vitrification, organic matters are corroded by organic acids to form organic pores, which are usually small, with a pore size of several hundred nanometers.

Fracture: In the observation of profile and core, interlayer bedding fractures with a low angle were found, with millimeter-level width, and partially filled. Under thin section observation and scanning electron microscope, many unfilled interbedded fractures were observed. Such fractures have a millimeter-level width and are common in tuffaceous mudstone.

According to the characteristics of pore in tuffaceous rocks, the pores at the formation under study can be classified into two scale levels. 1) Micron-scale: It mainly includes dissolution pores formed in pyroclast or carbonate minerals, with a size of about 0–50 μm . Dissolution pores in carbonate minerals are relatively small, generally with a size varying from 0 to 10 μm , as shown in Figure 4C. The largest dissolution pores in calcite are less than 10 μm . The pores locally found in tuff are also micron-scale pores. 2) Nano-scale: It mainly includes shrinkage pores between primary and secondary clay minerals, followed by micropores in organic matter and small dissolution pores on the surface of dolomite. According to the image of the scanning electron microscope,

nano-scale shrinkage pores in clay minerals are developed and with relatively high connectivity. Fractures, especially bedding fractures, are developed in rocks. They cannot only become reservoir spaces but also serve as effective channels for oil-gas migration. Therefore, a high fracture rate at the fracture face is an important factor for increased reservoir capacity of a rock formation. The directionality of the mixed argillaceous and clay products, as well as the laminae developed in tuffaceous rocks, can be the main cause for the development of bedding fractures.

5.2.2 Distribution characteristics of pore size

MICP experiment is an important means to observe the mercury inflow into/withdrawal from cores and pore throat distribution characteristics, and the experimental results are shown in Figure 7. For tuff, the displacement pressure is 107.487 MPa, the maximum connection radius 0.007 μm , the median pressure 242.215 MPa, the median radius 0.003 μm , the maximum mercury inflow saturation 100%, the residual mercury saturation 64.97%, and the mercury withdrawal efficiency 35.03%. For sedimentary tuff, the displacement pressure is 155.077 MPa, the maximum connection radius 0.005 μm , the median pressure 265.610 MPa, the median radius 0.003 μm , the maximum mercury inflow saturation 100%, the residual mercury saturation 76.71%, and the mercury withdrawal efficiency 23.29%. For tuffaceous mudstone, the displacement pressure is 55.465 MPa, the maximum connection radius 0.013 μm , the median pressure 209.764 MPa, the median radius 0.004 μm , the maximum mercury inflow saturation 100%, the residual mercury saturation 52.55%, and the mercury withdrawal efficiency 47.45%.

In general, the middle section of the mercury inflow curve of tuffaceous rock cores not only has a large span but also is relatively gentle, indicating that the pores in the core are concentrated. The displacement pressure is between 55.465 and 155.077 MPa, with an average value of 106.011 MPa; the maximum connection radius varies from 0.005 to 0.013 μm , with an average value of 0.008 μm ; the median pore throat radius varies from 0.003 to 0.004 μm , with an average value of 0.0033 μm . It indicates that the pores are generally of nano-scale. The maximum mercury inflow saturation

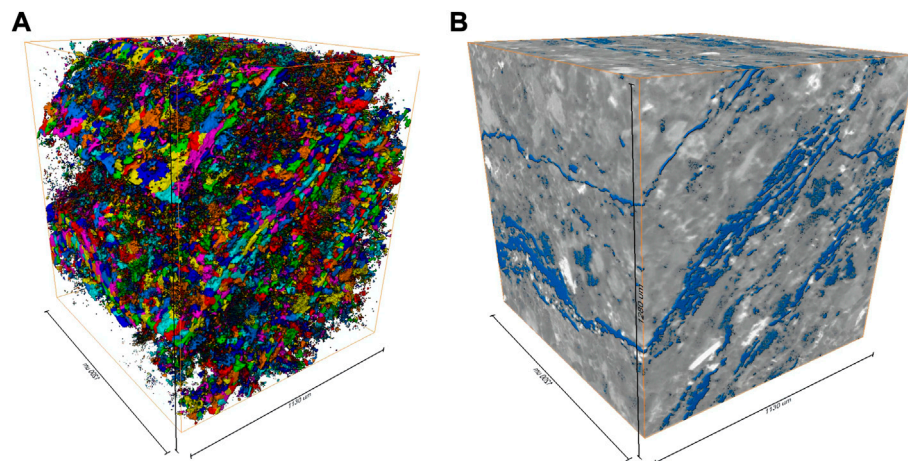


FIGURE 8

Micro-CT scan images (A) Different colors representing different organic matter and pore clusters; (B) Organic matter and pore segmentation).

of the core can reach 100%, indicating that the pore structure of the tight sedimentary tuff can be identified by the mercury injection method. Whereas, the mercury withdrawal efficiency of the core varies from 23.29% to 47.45%, with an average value of 35.26%, indicating an obvious effect of capillary pressure on the retention in the core pores, and such an effect is also an important reason for the low flowback rate of fracturing fluid and injected water in mines.

The frequency curve of the pore throat radius distribution of different cores is shown in Figure 7B. The most widely distributed pore scale in tuffaceous rock cores is $0.0036\ \mu\text{m}$, and the proportions of this scale in the total pores of each core are 47.3%, 33.1%, and 39.8%. The pore scale that follows is $0.002\ \mu\text{m}$, and the proportions of this scale in the total pores of each core are 13.1%, 32.4%, and 9.8%. The pores are generally nanopores.

5.2.3 Pore connectivity

After the 3D reconstruction of micro-CT images, each color represents a certain group of pores that are connected with each other (Figure 8). It can be seen that there are many throats in the samples of Permian tuffaceous rocks from the Sichuan Basin, the organic matter has obvious characteristics of lamina and is distributed with bedding fractures. The volume of organic matter and pores can reach 9.1%, indicating that the samples in this area have relatively high pore connectivity. Various types of pores and fractures are connected to each other to form complex organic-inorganic pore-fracture systems of connected networks and bedding fractures with higher connectivity, which become effective reservoirs with three-dimensional connectivity and lateral dominant channels along bedding fractures and provide the main storage spaces and flow channels for the enrichment and high production of oil and gas in tuffaceous rocks.

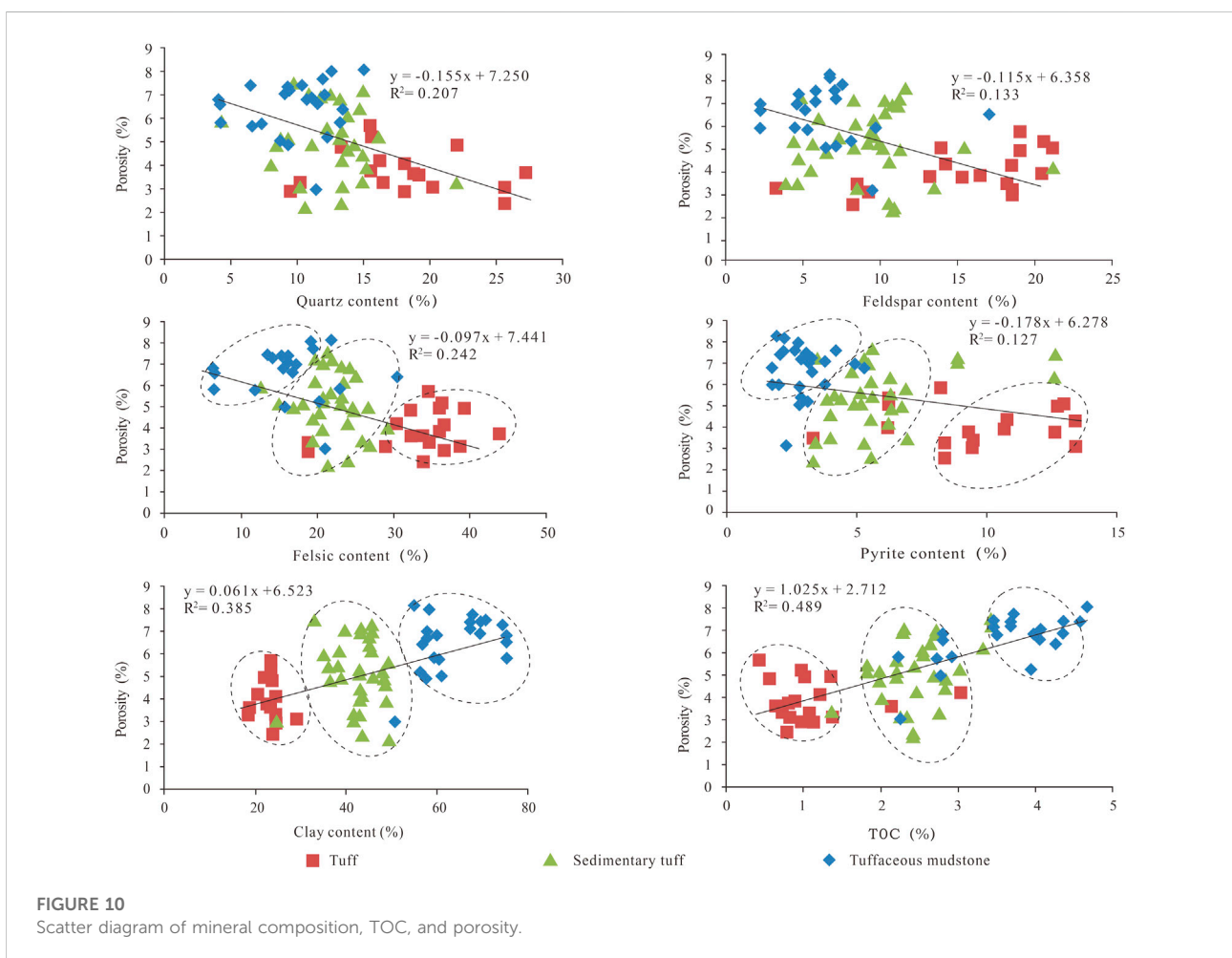
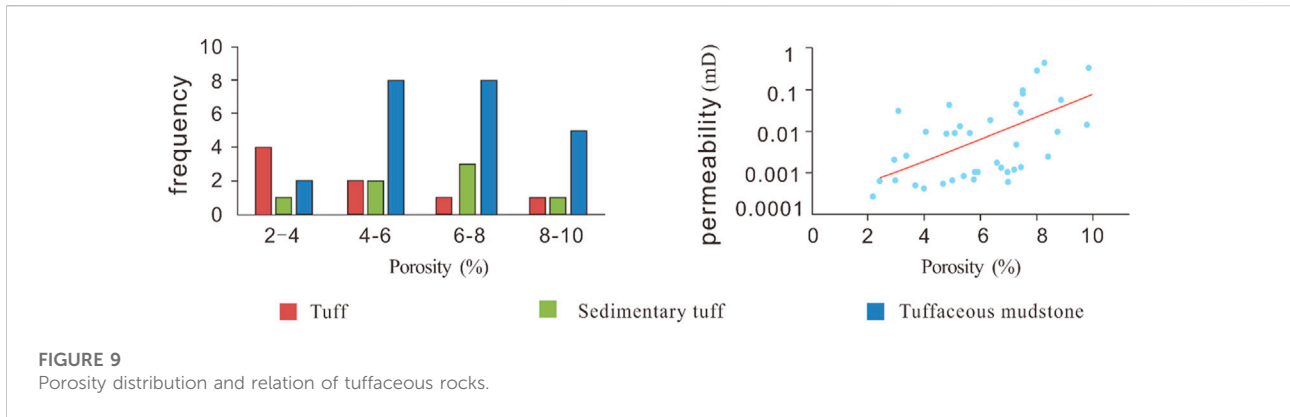
5.3 Factors affecting porosity

To identify factors affecting the porosity of the tuffaceous section, a large number of samples were selected for porosity testing and analysis. It is found that the tuffaceous section has a relatively high overall porosity, ranging between 2.2% and 8.1%, mostly concentrated in the range of 3%–7% and with an average value of 5.24% (Figure 9).

5.3.1 Correlation between mineral composition and pores

A large number of samples were selected to study the variation in mineral composition against the porosity of the tuffaceous section. According to the scatter diagram (Figure 10), when the quartz content is low, the porosity of the tuffaceous section is relatively high, and with the quartz content increasing, the porosity tends to decrease. No conspicuous connection is observed in the variation of the feldspar content against the porosity. Generally, the feldspar content is inversely correlated with the porosity variation, i.e., the lower the feldspar content, the higher the porosity. The variation of pyrite content is also inversely correlated with the porosity. When the pyrite content is low, the porosity is high. When the pyrite content exceeds 10%, the porosity varies inconspicuously. However, there is a significant positive correlation between clay content and porosity. When the clay content rises, the porosity increases accordingly.

To sum up, the analysis over changes in mineral composition and porosity shows that the higher the volcanic content, the lower the porosity; the higher the clay mineral content, the higher the porosity.



5.3.2 Correlation between TOC content and pores

Similar to shale, among pores of the tuffaceous section, shrinkage pores and fractures are frequently seen. It is

essential to answer such a question: whether the TOC content of the tuffaceous section will affect pores. Based on enormous sample analyses, it is found that in most cases, the tuffaceous section has a porosity higher than 2%, varying from 2.4% to 5.7%

TABLE 3 Pore size distribution of tuffaceous rocks.

Sample no.	Sample 1	Sample 2	Sample 3	Sample 4	Sample 5	Sample 6
Diameter (nm)	Pore size percentage					
<0.8	3.2%	3.5%	4.1%	2.5%	8.8%	2.2%
0.8–1.2	13.3%	18.8%	19.6%	21.8%	22.1%	24.7%
1.2–2	4.0%	3.5%	4.3%	3.9%	4.3%	4.2%
2–4	18.7%	14.4%	18.4%	16.9%	18.2%	17.5%
4–6	12.2%	9.7%	7.9%	9.6%	12.1%	14.1%
6–8	9.9%	8.3%	9.7%	8.2%	7.9%	4.0%
8–10	5.8%	5.6%	4.7%	5.6%	3.6%	11.0%
10–20	14.9%	12.3%	15.3%	15.6%	9.3%	9.5%
20–30	6.5%	8.2%	3.9%	5.6%	4.3%	4.1%
30–50	3.3%	4.0%	3.8%	2.9%	3.1%	3.2%
50–80	1.4%	2.8%	2.0%	1.3%	1.2%	0.9%
80–120	0.7%	0.5%	0.8%	0.6%	0.3%	0.3%
120–180	0.7%	1.2%	0.5%	0.4%	0.5%	0.4%

when the TOC content is smaller than 1%, with an average value of 3.85. As the TOC content increases, however, the porosity tends to grow (Figure 10).

5.3.3 Correlation between lithofacies and pores

Different lithofacies types differ in their formation environments. The tuffaceous section in this study has three lithofacies types: tuff, sedimentary tuff, and tuffaceous mudstone. From the distribution in the scatter diagram, the mineral composition varies greatly among the three lithofacies types. Among them, tuff sees a high content of felsic rocks and pyrite and a low content of clay. Holistically, tuffaceous mudstone contains more clay and less felsic rocks and pyrite. Tuff has a low porosity between 2.4% and 5.7%, mainly concentrated in 3%–4% and averaging 3.86%; sedimentary tuff has a porosity between 2.2% and 7.5%, mainly concentrated in 3%–7% and averaging 5.09%; tuffaceous mudstone has the highest porosity between 5% and 8%, averaging 6.5%. Among the three lithofacies, the porosity is greatly affected by the mineral composition, and the change of clay content is obviously affected by the lithofacies. Tuff, with the lowest clay content, sees the lowest average porosity. Tuff, with the lowest TOC content, sees the lowest porosity, while tuffaceous mudstone, with the highest clay and TOC, sees the highest average porosity.

5.4 Mineral enrichment

From the traditional logging and core library data, fine-grained sediments in this section mainly include argillaceous

limestone, marlstone, and mudstone. According to the whole-rock XRD data, this section contains stable volcanic ash, mostly felsic rocks, and the volcanic ash has a good positive correlation with the pyrite content. As well as the association of volcanic materials with pyrite manifested by the lithology of this section in the Permian System of the Sichuan Basin, volcanic materials are also frequently seen in pyrite in many other parts around the world. The volcanic origin is an important formation mechanism for this type of ore (Jones and Gislason, 2008; Song et al., 2018; Jiang, 2019). Pyrite, also FeS₂, provides a source of sulfur (dominant action) or iron because of the genetic relations between volcanic materials and pyrite. The source of sulfur mainly comes from the sulfur components stored in magma, which are transported to the seawater through volcanic eruptions. In the southwest Sichuan Basin, intense volcanic eruption emits volcanic ash clouds containing abundant gaseous SO₂. During the intermission time, the crater and nearby developed volcanic fumarole can still vent gaseous SO₂ steadily and incessantly, and such strong acid gases, coupled with volcanic ash, are ejected in the form of ash clouds. Under a high temperature, sulfur aerosols and sulfuric acid (from oxidation of SO₂) are highly corrosive to the surface of volcanic ash, forming a sulfate-contained salt film on the surface (Zhang H. F. et al., 2006; Jones and Gislason, 2008). Within a short time after going into seawater, volcanic ash can release a torrent of sulfate ions. In the north and the east of Sichuan, underwater crater eruption is the prevailing case. Since lava is easier to react with seawater, SO₂ in lava is directly dissolved in seawater after degassing from lava, increasing the content of sulfate ions in the water body.

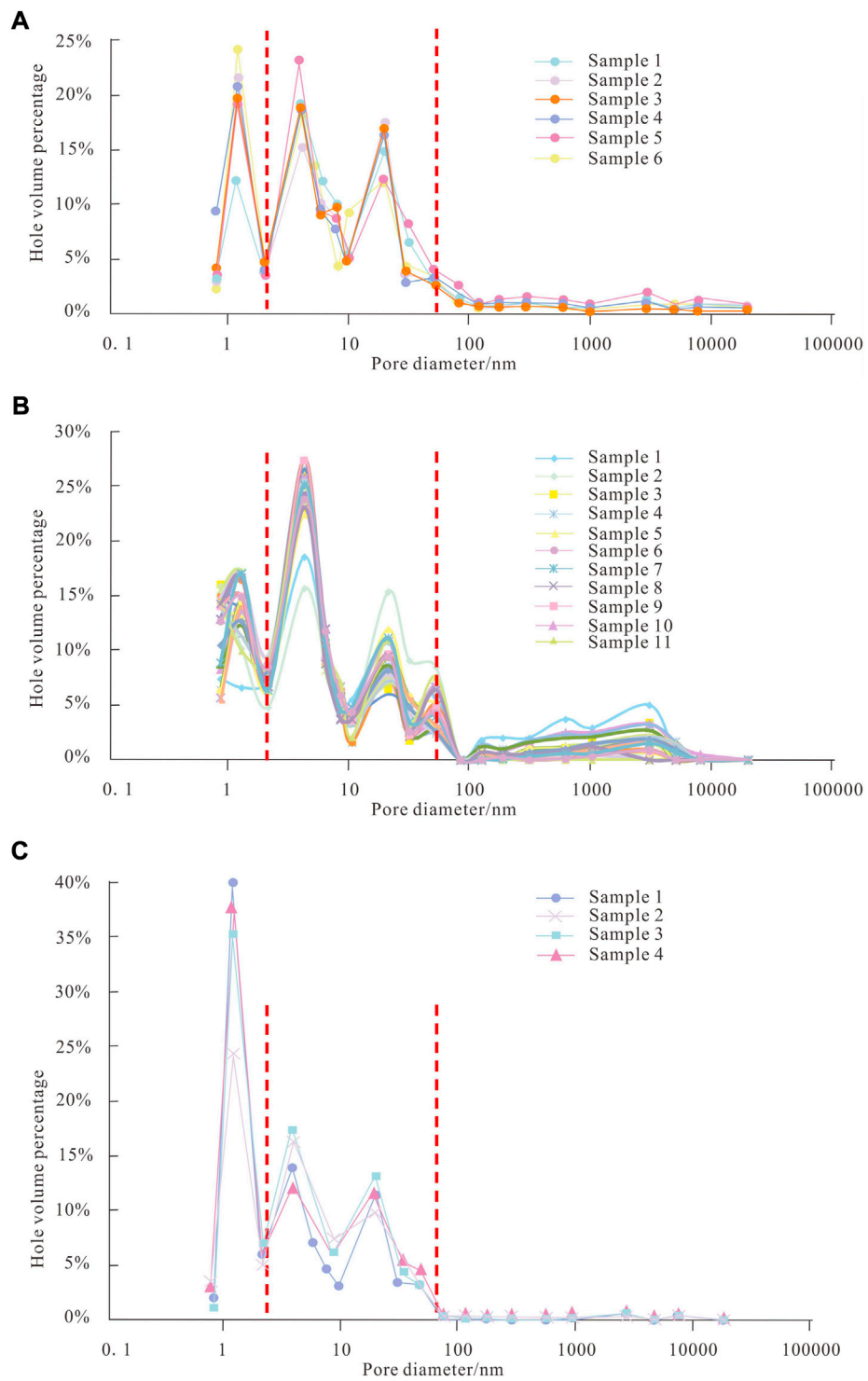


FIGURE 11

Comparison of pore size distribution of tuffaceous rocks and shale in the sichuan basin (A) Pore size distribution of tuffaceous rock in wujiaping formation; (B) Pore size distribution of shale in longmaxi formation; (C) Pore size distribution of shale in dalong formation.

The clay content in the tuffaceous rock section in the study area is obviously enriched. The clay mineral content in the section of Hongyan Township is up to 75%, and the content of smectite mixed layer in the clay mineral is high, XRD Data of Clay for Tuffaceous Section of Hongyan Township profile shows that this sample contains the same clay mineral composition as the clay mineral assemblage in the clay rock of volcanic origin at the Permian-Triassic boundary in other parts of South China, featuring thin stratification and uniform thickness (Zhang S. X. et al., 2006).

5.5 Comparison of pores in tuffaceous section and shale

Previous studies have shown that shale reservoirs are dominated by nanoscale organic pores and intergranular pores, with a small number of intragranular pores and a small number of nanoscale fractures. Among them, mineral intercrystalline pores and pores in organic matter constitute the most effective pore network that provides sufficient storage space for abundant shale gas resources. In the study of shale pore structure, it is found that both micropores and mesopores are developed in shale, and macropores are less developed (Curbs, 2002; Zou et al., 2011; Liu et al., 2013).

According to the classification standard of pores by the International Union of Pure and Applied Chemistry (IUPAC) (IUPAC, 1994), the MICP experiment can be jointly used for quantitative characterization of pores of different sizes in samples (micropores <2 nm, mesopores 2–50 nm, macropores >50 nm) (Cao et al., 2015). The test results of six samples of Daping Village profile of Permian tuffaceous rocks in the Sichuan Basin are shown in Table 3. The pore size distribution shows that the pores in the samples are mainly micropores and mesopores, and the pores with a size <50 nm account for 88.3–94.5%, with an average value of 92.12%. Among them, micropores account for 28.1% of all pores of the samples and mesopores 64.02%; the macropores account for 5.5%–11.7% of the pores of six samples, with an average value of 7.88%.

The tuffaceous section is a set of tight rock sections. To further clarify the pore characteristics of Permian tuffaceous rocks in the Sichuan Basin, they are compared with the pore characteristics of tight shale. A total of four core samples of Dalong Formation shale from typical wells and 11 core samples of Longmaxi Formation shale from typical wells in the Sichuan Basin are selected for pore size analysis (Figure 11). It is found that the pores of Longmaxi shale are mainly micropores and mesopores, with an average proportion of 37.2% and 51.5 respectively, and the average proportion of macropores can reach 11.3%. Compared with Longmaxi Formation, Longtan Formation shale has a quite different pore size distribution, with its micropores being developed and accounting for 43.7%, its mesopores accounting for 55.1% and its macropores basically being not developed and accounting for only 1.2%.

According to the comparison of the pore size distribution of the tuffaceous section and the typical shale section in the area under study, micropores and mesopores are the major pores in core samples, accounting for about 90%, and macropores are relatively less developed. The overall trend of the pore size distribution of the tuffaceous rock section and shale is basically consistent.

In general, both the tuffaceous section and shale are tight, and the pores are mainly nano-scale and micro-scale. In terms of pore structure, micropores and mesopores are the major pores, and macropores are less developed. The organic-inorganic pores and fractures are connected to form a pore-fracture network system in the tight formation, providing sufficient storage space for abundant oil and gas resources.

6 Conclusion

In this paper, the author focuses on the tuffaceous section in the new field of marine facies and identifies four points by studying the lithofacies, minerals, and pore characteristics by means of field outcrop, thin section, scanning electron microscope, XRD, MICP, CT scan, and other experiments.

- 1) The Permian marine tuffaceous section in the Sichuan Basin mainly consists of three lithofacies types: tuff, sedimentary tuff, and tuffaceous mudstone. The tuff contains 75%–90% pyroclast, with no obvious stratified structures. The sedimentary tuff and tuffaceous mudstone are often interbedded and stratified. The sedimentary tuff contains 50%–75% pyroclast, with a terrigenous clast content of no more than 50%. The tuffaceous mudstone, however, contains more than 50% clay and less than 10% pyroclast. The mineral composition of the tuffaceous section includes quartz, feldspar (mostly plagioclase), carbonate minerals, pyrite, clay, etc. The quartz content varies from 4.0% to 27.3%, with an average value of 13.0%; the feldspar content varies from 0 to 21.2%, with an average value of 9.8%; the carbonate mineral content varies from 8.52% to 53.45%, with an average value of 27.6%; the clay mineral content varies from 0% to 75.3%, with an average value of 44.8%, and the pyrite content varies from 0 to 13.4%, with an average value of 5.8%.
- 2) The pores of the tuffaceous section mainly include shrinkage pores, dissolution pores, intercrystalline pores, and organic pores. In terms of their scales, they can be divided into micron-scale and nano-scale pores. The micro-scale pores have a size of about 0–50 μm and mainly include dissolution pores and air pores; the nano-scale pores include shrinkage pores and organic-matter pores. Fractures in the tuffaceous section, especially bedding fractures, are relatively developed. In terms of the pore size of the tuffaceous section, the pores are mainly micropores and mesopores, and the pores of samples with a size <50 nm account for 88.3–94.5%, with an average value of 92.12%. Among them, micropores account for 28.1% of all pores of the samples and

mesopores 64.02%; the macropores account for 5.5%–11.7%, with an average value of 7.88%. The pores in the cores are distributed in a concentrated way and are well-connected with each other. Various types of pores and fractures are interconnected to form complex organic-inorganic pore-fracture systems of connected networks and bedding fractures with higher connectivity.

- 3) The porosity of the tuffaceous section is relatively high, with the minimum exceeding 2%, ranging between 2.2% and 8.1% on the whole, mostly concentrated in 3%–7% and with an average of 5.24%. The pores of the tuffaceous section are greatly affected by lithofacies and mineral composition. The tuff has a low porosity between 2.4% and 5.7%, mainly concentrated in 3%–4% and averaging 3.86%; the sedimentary tuff has a porosity between 2.2% and 7.5%, mainly concentrated in 3%–7% and averaging 5.09%; tuffaceous mudstone has the highest porosity between 5% and 8%, averaging 6.5%. The higher the total content of feldspar and quartz, the lower the porosity, that is, the felsic content is inversely correlated with the porosity. The higher the clay content, the higher the porosity; the higher the TOC content, the higher the porosity; the clay content and TOC content are both positively correlated to the porosity. The higher the pyrite content, the lower the porosity, that is, the pyrite content is inversely correlated with the porosity.
- 4) The marine tuffaceous section is similar to shale to a certain extent as it has relatively dense lithology, and its pores are mainly of micron-scale and nano-scale and mainly include micropores and mesopores. It boasts hydrocarbon-generating capacity and reservoir performance, serving as both a source rock and a reservoir. As a novel reservoir, the tuffaceous section can form a tight reservoir both generating and depositing gas and featuring source-reservoir paragenesis, lithological reservoir-controlling, and large-area stratified distribution, manifesting a promising future for exploration.

Data availability statement

The original contributions presented in the study are included in the article/supplementary material, further inquiries can be directed to the corresponding author.

References

- Ali, J. R., Thompson, G. M., Song, X. Y., and Wang, Y. L. (2002). Emeishan basalts (SW China) and the 'end-guadalupian' crisis: Magnetobiostratigraphic constraints. *J. Geol. Soc. Lond.* 159 (1), 21–29. doi:10.1144/0016-764901086
- Altaner, S. P., and Ylagan, R. F. (1997). Comparison of structural models of mixed-layer illite/smectite and reaction mechanisms of smectite illitization. *Clays Clay Min.* 45, 517–533. doi:10.1346/CCMN.1997.0450404

Author contributions

Author Contributions Conceptualization, RL, ZW; result analysis, RL, ZW; Experiments, ZX, WX; Field observation and sample collection, WL; Structural settings, NS. All authors have read and agreed to the published version of the manuscript.

Funding

This research was supported by the Major Scientific and Technological Project of PetroChina (Grant Nos. 2021DJ0605).

Acknowledgements

The author sincerely thanks the Research Center of Sichuan Basin of PetroChina Research Institute of Petroleum Exploration & Development, Sinopec Exploration Company and PetroChina Southwest Oil & Gasfield Company, Chengdu, China, for providing core samples and basic geological data, and the experimental support provided by the experimental center of Chengdu University of Technology, Chengdu, China.

Conflict of interest

The authors RL, ZW, WX and NS were employed by Research Institute of Petroleum Exploration & Development, PetroChina. The author ZX was employed by Sinopec Exploration Company.

The remaining author declares that the research was conducted in the absence of any commercial or financial relationships that could be construed as a potential conflict of interest.

Publisher's note

All claims expressed in this article are solely those of the authors and do not necessarily represent those of their affiliated organizations, or those of the publisher, the editors and the reviewers. Any product that may be evaluated in this article, or claim that may be made by its manufacturer, is not guaranteed or endorsed by the publisher.

- Bertog, J., Huff, W., and Martin, J. E. (2007). Geochemical and mineralogical recognition of the bentonites in the lower Pierre Shale Group and their use in regional stratigraphic correlation [M]. *Geol. Soc. Am. Special Pap.* 427, 23–50. doi:10.1130/2007.2427(03)

- Cao, T., Song, Z., Wang, S., Cao, X., Li, Y., and Xia, J. (2015). Characterizing the pore structure in the silurian and permian shales of the Sichuan basin, China. *Mar. Petroleum Geol.* 61, 140–150. doi:10.1016/j.marpetgeo.2014.12.007

- Cao, Y. C., Jiang, Z. X., and Qiu, L. W. (1999). Study on the type and origin of the reservoir space of igneous oil reservoir in Shang 741 Block, Huimin Depression, Shandong [J]. *Acta Petrol. Sin.* 15 (1), 129–136.
- Carey, R. J., Houghton, B. F., and Thordarson, T. (2008). Contrasting styles of welding observed in the proximal Askja 1875 eruption deposits I: Regional welding. *J. Volcanol. Geotherm. Res.* 171, 1–19. doi:10.1016/j.jvolgeores.2007.11.020
- Chalmers, G. R., Bustin, R. M., and Power, I. M. (2012). Characterization of gas shale pore systems by porosimetry, pycnometry, surface area, and field emission scanning electron microscopy/transmission electron microscopy image analyses: Examples from the Barnett, Woodford, Haynesville, Marcellus, and Doig units. *Am. Assoc. Pet. Geol. Bull.* 6 (96), 1099–1119. doi:10.1306/10171111052
- Chen, L., Jiang, Z., Liu, K., Wang, P., Ji, W., Gao, F., et al. (2016). Effect of lithofacies on gas storage capacity of marine and continental shales in the Sichuan Basin, China. *J. Nat. Gas Sci. Eng.* 36, 773–785. doi:10.1016/j.jngse.2016.11.024
- Cheng, R. H., Shen, Y. J., Yan, J. B., Li, Q. F., Li, X. H., Wang, Y. W., et al. (2010). Diagenesis of volcanoclastic rocks in Hailaer basin [J]. *Acta Petrol. Sinica* 26, 47–54.
- Christidis, G. E., and Huff, W. D. (2009). Geological aspects and genesis of bentonites. *Elements* 5, 93–98. doi:10.2113/gselements.5.2.93
- Chung, F. H. (1974). Quantitative interpretation of X-ray diffraction patterns of mixtures. I. Matrix-flushing method for quantitative multicomponent analysis. *J. Appl. Crystallogr.* 7, 519–525. doi:10.1107/S0021889874010375
- Colin, W. J. N., and Wes, H. (2003). Assembling an ignimbrite: Mechanical and thermal building blocks in the bishop tuff, California [J]. *J. Geol.* 111, 653–670. doi:10.1111/j.1365-2362.2008.01963.x
- Curbs, J. B. (2002). Fractured shale-gas systems. *Am. Assoc. Pet. Geol. Bull.* 86 (11), 1921–1938. doi:10.1306/61EEDDBE-173E-11D7-8645000102C1865D
- Ddani, M., Meunier, A., Zahraoui, M., Beaufort, D., El Wartiti, M., Fontaine, C., et al. (2005). Clay mineralogy and chemical composition of bentonites from the Gourougou volcanic massif (northeast Morocco). *Clays Clay Min.* 53, 250–267. doi:10.1346/CCMN.2005.0530305
- Deconinck, J. F., Crasquin, S., Bruneau, L., Pellenard, P., Baudin, F., and Feng, Q. (2014). Diagenesis of clay minerals and K-bentonites in late Permian/early Triassic sediments of the Sichuan basin (Chaotian section, Central China). *J. Asian Earth Sci.* 81, 28–37. doi:10.1016/j.jseas.2013.11.018
- Fan, X. Y., He, L., Zhang, Q. G., Zhao, P. F., Zhang, M. M., Yao, B. W., et al. (2022). Effect of hydration on pore structure and physical properties of permian basalt and tuff in Sichuan basin during pressurized imbibition. *J. Petroleum Sci. Eng.* 213, 110322. doi:10.1016/j.petrol.2022.110322
- Freundt, A. (1999). Formation of high-grade ignimbrites Part II. A pyroclastic suspension current model with implications also for low-grade ignimbrites. *Bull. Volcanol.* 60, 545–567. doi:10.1007/s0044500505251
- Garcia-Romero, E., Vegas, J., Baldonado, J. L., and Marfil, R. (2005). Clay minerals as alteration products in basaltic volcanoclastic deposits of La Palma (Canary Islands, Spain). *Sediment. Geol.* 174, 237–253. doi:10.1016/j.sedgeo.2004.12.007
- Gecer, B. A. (2006). Diagenesis of tipper Eocene volcanoclastic rocks and its relevance to hydrocarbon exploration in the Thrace Basin, Turkey[J]. *Energy Sources, Part A* (11), 1039–1049. doi:10.1080/00908310500278797
- He, J., Zheng, R. C., Hu, X., Zhang, B. J., Yin, H., Ma, H. L., et al. (2015). Sedimentary system of the late permian Wujiaping Formation in the Western Sichuan basin [J]. *Oil Gas Geol.* 36 (1), 87–95. doi:10.11743/ogg20150111
- Hickey, J. J., and Henk, B. (2007). Lithofacies summary of the mississippian barnett shale, mitchell 2 T.P. Sims well, wise county, Texas. *Am. Assoc. Pet. Geol. Bull.* 91 (4), 437–443. doi:10.1306/12040606053
- Hong, Z., Zhu, W. G., Hu, R. Z., Xie, L. W., He, D. F., Feng, L., et al. (2009). Zircon U–Pb age and Sr–Nd–Hf isotope geochemistry of the Panzhihua A-type syenitic intrusion in the Emeishan large igneous province, southwest China and implications for growth of juvenile crust. *Lithos* 110, 109–128. doi:10.1016/j.lithos.2008.12.006
- Hu, D. F. (2019). Breakthrough in natural gas exploration in the platform margin shoal at the Maokou Fm in the Yuanba area, Sichuan Basin, and its implications [J]. *Oil Gas Geol.* 39 (3), 1–10. doi:10.3787/j.issn.1000-0976.2019.03.001
- Huang, H., Cawood, P. A., Hou, M. C., Ni, S. J., Yang, J. H., Du, Y. S., et al. (2018). Provenance of late permian volcanic ash beds in south China: Implications for the age of emeishan volcanism and its linkage to climate cooling. *Lithos* 314, 293–306. doi:10.1016/j.lithos.2018.06.009
- Huang, K., and Opdyke, N. D. (1998). Magnetostratigraphic investigations on an Emeishan basalt section in Western Guizhou province, China. *Earth Planet. Sci. Lett.* 163 (1–4), 1–14. doi:10.1016/S0012-821X(98)00169-1
- Inoue, A., Meunier, A., and Beaufort, D. (2004). Illite-smectite mixed-layer minerals in felsic volcanoclastic rocks from drill cores, kakkonda, Japan. *Clays Clay Min.* 52, 66–84. doi:10.1346/CCMN.2004.0520108
- IUPAC (International Union of Pure and Applied chemistry) (1994). Physical Chemistry division commission on colloid and surface Chemistry, subcommittee on characterization of porous solids. Recommendations for the characterization of porous solids (technical report) [J]. *Pure Appl. Chem.* 66 (8), 1739–1758.
- Jiang, Z. F. (2019). *Influence of volcanic ash on Source rock organic matter enrichment in the Lucaogou Formation, the Jimusar Depression [D]*. Beijing: China University of Petroleum.
- Jones, M. T., and Gislason, S. R. (2008). Rapid releases of metal salts and nutrients following the deposition of volcanic ash into aqueous environments. *Geochimica Cosmochimica Acta* 72 (15), 3661–3680. doi:10.1016/j.gca.2008.05.030
- Levin, L. E. (1995). Volcanogenic and volcanoclastic reservoir rocks in Mesozoic-Cenozoic island arcs: Examples from the Caucasus and the NW Pacific [J]. *J. Petroleum Geol.* 18 (3), 267–288. doi:10.1306/BF9AB759-0EB6-11D7-8643000102C1865D
- Li, M. X., Qu, H. Z., Zeng, Q., Yin, H., Zhang, Y. F., Liu, M. Y., et al. (2020). Pore evolution characteristics and distribution of favorable reservoir area of the upper permian Wujiaping Formation in the northwestern sichuan [J]. *Nat. Gas. Geosci.* 31 (11), 1574–1584. doi:10.11764/j.issn.1672-1926.2020.08.009
- Li, Q., Lu, H., Li, J., Wu, S., Wu, Y., Wen, L., et al. (2022). Characteristics and formation mechanism of the tight tuff reservoirs of the upper triassic chang 7 member in the southern Ordos Basin, China. *SSRN J.* 139, 105625. doi:10.2139/ssrn.4003891
- Liu, K. L., Yang, S., Chen, H. D., Li, Q., Ma, L., and Zhang, C. G. (2020). Characteristics and evolution of Permian volcanic rocks in Huayingshan area, eastern Sichuan basin [J]. *Mineral Petrology* 40 (1), 37–49. doi:10.19719/j.cnki.1001-6872.2020.01.05
- Liu, S. G., Ma, W. X., Lubomir, J., Huang, W. M., Zeng, X. L., and Zhang, C. (2013). Characteristics of the shale gas reservoir rocks in the lower silurian Longmaxi Formation, east Sichuan basin, China. *Energy Explor. Exploitation* 31 (2), 187–219. doi:10.1260/0144-5987.31.2.187
- Liu, W. Z., Pang, Y. M., Wu, H. Y., Gao, Y. F., Men, G. T., and Ren, Y. G. (2007). Relationship between pore-space evolution and deeply buried alteration during diagenetic stage of the volcanic fragments in reservoir greywacke from the Songliao Basin, NE China [J]. *Earth Sci. Ed.* 37, 698–702. doi:10.13278/j.cnki.jjuese.2007.04.014
- Ma, X. H., Xu, C. C., Li, G. H., Ying, D. L., Zhang, B. J., Li, Y., et al. (2019a). Distribution and gas bearing properties of Permian igneous rocks in Sichuan Basin SW China [J]. *Petroleum Explor. Dev.* 46 (2), 216–225. doi:10.11698/PED.2019.02.03
- Ma, X. H., Yang, Y., Zhang, J., and Xie, J. R. (2019b). A Major discovery in Permian volcanic rock gas reservoir exploration in the Sichuan Basin and its implications[J]. *Oil Gas Geol.* 39 (2), 1–8. doi:10.3787/j.issn.1000-0976.2019.02.001
- Moore, D. M., and Reynolds, R. C. (1998). *X-ray diffraction and the identification and analysis of clay minerals*[J]. New York: Oxford University Press. Earth science Reviews. doi:10.1016/S0012-8252(97)00020-2
- Peate, I. U., and Bryan, S. E. (2008). Re-evaluating plume-induced uplift in the Emeishan large igneous province. *Nat. Geosci.* 1 (9), 625–629. doi:10.1038/ngeo281
- Peng, H., Yin, C., He, Q. L., Xia, G. Y., Liu, Yong., Ma, T. H., et al. (2022). Development characteristics and petroleum geological significance of Permian pyroclastic flow volcanic rocks in Western Sichuan Basin, SW China [J]. *Petroleum Explor. Dev.* 49 (1), 56–67.
- Schmid, R. (1981). Descriptive nomenclature and classification of pyroclastic deposits and fragments. *Geol. Rundsch.* 70, 794–799. doi:10.1007/BF01822152
- Schutter, S. R. (2003). Occurrences of hydrocarbons in and around igneous rocks. *Geol. Soc. Lond. Spec. Publ.* 214 (1), 35–68. doi:10.1144/GSL.SP.2003.214.01.03
- Shellnutt, J. G., Denyszyn, S. W., and Mundil, R. (2012). Precise age determination of mafic and felsic intrusive rocks from the Permian Emeishan large igneous province (SW China). *Gondwana Res.* 22 (1), 118–126. doi:10.1016/j.gr.2011.10.009
- Song, G. X., Qin, K. Z., Li, G. M., and Wang, L. (2018). Basic characteristics and research progresses of intermediate sulfidation type epithermal gold poly-metallic deposits, and prospects [J]. *Acta Petrol. Sin.* 34 (3), 748–762.
- Streck, M. J., and Grunder, A. L. (1995). Crystallization and welding variations in a widespread ignimbrite sheet: The rattlesnake tuff, eastern Oregon, USA[J]. *Bull. Volcanol.* 60 (7), 545–567. doi:10.1007/BF00265035
- Syed, M. I., and Padmanabhan, E. (2022). Lithofacies, mineralogy, and pore types in Paleozoic gas shales from Western Peninsular Malaysia [J]. *J. Petroleum Sci. Eng.* 212, 110239. doi:10.1016/j.petrol.2022.110239
- Tian, J., Lin, X., Guo, W., Zhang, X., and Huang, P. (2017). Geological significance of oil and gas in the eruption event in Sichuan Basin Permian basalt China [J]. *J. Cheng du Univ. Technol. Sci. Technol. Ed.* 44 (1), 14–20. doi:10.3969/j.issn.1671-9727.2017.01.02

- Tian, X. W., Luo, B., Sun, Y. T., Liu, R., Li, Y., Chen, Y. Q., et al. (2021). Natural gas characteristics and source analysis of permian volcanic gas reservoir: A case study of well YT1 in chengdu-jianyang area, Sichuan basin[J]. *J. Jilin Univ. (Earth Sci. Ed. 51* (2), 325–335.
- Tian, Y. (2018). *Lithofacies palaeogeography of the upper permian wujiaping period in the Sichuan basin*[D]. Beijing: China University of Geosciences.
- Tian, Y., Zhang, X. Y., He, Y. B., Luo, J. X., Zhou, H., Zhou, X. P., et al. (2010). Lithofacies paleogeography of late permian wujiapingage in Sichuan basin [D]. *J. Paleogeogr.* 12 (2), 164–176.
- Vernik, L. (1990). A new type of reservoir rock in volcanoclastic sequences (1). *Am. Assoc. Pet. Geol. Bull.* 74 (6), 830–836. doi:10.1306/0C9B23A3-1710-11D7-8645000102C1865D
- Wang, H. Y., Liu, L., Gao, Y. Q., and Zhang, X. T. (2005). Discussion of diageneses of volcanoclastic rocks of Nantun Format ion in Beier sags, Hailar basin[J]. *World Geol.* 24, 219–224.
- Wang, W. W., Jang, Z. X., Xie, X. Y., Guo, J. X., and Yang, Y. P. (2020). Sedimentary characteristics and interactions among volcanic, terrigenous and marine processes in the late permian kuishan member, eastern block of the north China craton. *Sediment. Geol.* 407, 105741. doi:10.1016/j.sedgeo.2020.105741
- Wen, L., Li, Y., Yi, H. Y., Liu, X., Zhang, B. J., Qiu, Y. C., et al. (2019). Lithofacies and reservoir characteristics of Permian volcanic rocks in the Sichuan Basin [J]. *Oil Gas Geol.* 39 (2), 17–27. doi:10.3787/j.issn.1000-0976.2019.02.003
- Wignall, P. B., Sun, Y., Bond, D. P. G., Izon, G., Newton, R. J., Veldre, S., et al. (2009). Volcanism, mass extinction, and carbon isotope fluctuations in the middle permian of China. *Science* 342 (29), 1179–1182. doi:10.1126/science.1171956
- Xia, M. L., Wen, L., Li, Y., Luo, B., He, K. L., Liu, R., et al. (2020). Permian volcanic eruption cycle, environment and model in the Jianyang area of the Sichuan Basin [J]. *Oil Gas Geol.* 40 (9), 11–22. doi:10.3787/j.issn.1000-0976.2020.09.002
- Xiang, F., Yu, X., Huang, H., Zhang, D., and Zhu, X. (2021). Mineralogical characterization and diagenetic history of Permian marine tuffaceous deposits in Guangyuan area, northern Sichuan basin, China. *Mar. Petroleum Geol.* 123, 104744. doi:10.1016/j.marpetgeo.2020.104744
- Yanik, G., Esenli, F., Uz, V., Esenli, V., Uz, B., and Kuelah, T. (2010). Ceramic properties of kaolinized tuffaceous rocks in Kesan region, Thrace, NW Turkey. *Appl. Clay Sci.* 48 (3), 499–505. doi:10.1016/j.clay.2010.02.014
- Zeng, Q., Tian, Y. Y., Zheng, C., Wang, X. L., and Li, R. R. (2020). Distribution of sedimentary tuff in Wujiaping Formation, northwestern Sichuan Basin and its geological significance [J]. *Nat. Gas Technol. Econ.* 14 (3), 20–26. doi:10.3969/j.issn.2095-1132.2020.03.004
- Zhang, H. F., Wu, X. S., Wang, B., Duan, Y. J., Qu, Y., and Chen, D. F. (2006). Research progress of the enrichment mechanism of sedimentary organics in lacustrine basin [J]. *Acta Sedimentol. Sin.* 34 (03), 463–477. doi:10.14027/j.cnki.cjxb.2016.03.004
- Zhang, J., Liu, G., Cao, Z., Tao, S., Felix, M., Kong, Y., et al. (2019). Characteristics and formation mechanism of multi-source mixed sedimentary rocks in a saline lake, a case study of the Permian Lucaogou Formation in the Jimusaer Sag, northwest China. *Mar. Petroleum Geol.* 102, 704–724. doi:10.1016/j.marpetgeo.2019.01.016
- Zhang, S. X., Feng, Q. L., Gu, S. Z., and Yu, J. S. (2006). Clay stone around deep water Permian-Triassic boundary from Guizhou and Guangxi Region [J]. *Geol. Sci. Technol. Inf.* 25 (01), 9–13.
- Zhang, X. T., Liu, L., and Wei, W. Y. (2008). Diagenesis and its influence to porosity evolution of tongbomiao formation in beier sag, hailar basin [J]. *J. Jilin Univ.* 38 (1), 34–42. doi:10.3969/j.issn.1671-5888.2008.01.005
- Zhang, Z. (2006). Geochemistry of picritic and associated basalt flows of the western emeishan flood basalt province, China. *J. Petrology* 47, 1997–2019. doi:10.1093/petrology/egl034
- Zhao, J. Q. (2019). *Diagenesis of volcanoclastic rocks and its effect on evolution of reservoir porosity: A case study of lower cretaceous in wujiapu depression* [D]. Changchun: Jilin University.
- Zhong, H., Zhu, W. G., Chu, Z. Y., He, D. F., and Song, X. Y. (2007). Shrimp U–Pb zircon geochronology, geochemistry, and Nd–Sr isotopic study of contrasting granites in the Emeishan large igneous province, SW China. *Chem. Geol.* 236, 112–133. doi:10.1016/j.chemgeo.2006.09.004
- Zhou, M. F., Malpas, J., Song, X. Y., Robinson, P. T., Sun, M., Kennedy, A., et al. (2001). A temporal link between the Emeishan large igneous province (SW China) and the end-Guadalupian mass extinction. *Earth Planet. Sci. Lett.* 196, 113–122. doi:10.1016/S0012-821X(01)00608-2
- Zhu, J., Zhang, Z. C., Wang, C., Tu, R., Jiang, J., and Lu, W. (2013). The link between large igneous provinces and the two mass extinction events in permian: Review of recent progress the permian [J]. *Expert Rev. Anticancer Ther.* 1 (59), 137–141. CNKI: SUN: DZLP.0.2013-01-019. doi:10.1586/era.12.145
- Zou, C. N., Zhu, R. K., Bai, B., Yang, Z., Wu, S. T., Su, L., et al. (2011). First discovery of nano-pore throat in oil and gas reservoir in China and its scientific value [J]. *Acta Petrol. Sin.* 27 (06), 1857–1864. CNKI:SUN:YSXB.0.2011-06-024.